Morphology Transitions of Twisted Ribbons: Dependence on Tension and Geometry

Hao Liu[1], Lei Liu[1], Zhi Yan[1,2], Yuming He[1,2], David J. Dunstan[3], Dabiao Liu[1,2*]

[1]Department of Engineering Mechanics, School of Aerospace Engineering, Huazhong University of Science and Technology, Wuhan 430074, China

[2]Hubei Key Laboratory of Engineering Structural Analysis and Safety Assessment, Wuhan 430074, China

[3] School of Physics and Chemical Sciences, Queen Mary University of London, London E1 4NS, UK

*Corresponding author: Prof. Dabiao Liu

E-mail: dbliu@hust.edu.cn

ABSTRACT

Slender ribbons can be stretched, bent, and twisted, exhibiting a range of complex morphologies. We study the morphology transitions of the ribbon subjected to tension and torsion by combining experiment and theory. A unified phase diagram as a function of torque and aspect ratio is constructed by comparing the microscopic and macroscopic buckling. Two distinct types of shape evolutions are identified. For the twist of a wide ribbon, the shape transforms from the helicoid through the crease to the cylinder. But for a narrow ribbon under torsion, no crease occurs. The mechanical behavior of the stretched and twisted ribbon is described based on the energy method. It is found that the succession of transformations for the morphologies strongly depends on the aspect ratio and tension. This study sheds light on understanding the morphological complexity of the constrained slender structure.

Slender ribbons are fundamental structures playing a pivotal role in the mechanical behavior of various synthetic and biological materials [1-4]. They have been used to design lightweight structures that can adapt their shapes in response to external stimulations [5, 6], in particular, under simultaneous axial tension and torsion. While a round rod or filament (aspect ratio unity) undergoes only macroscopic buckling to form a plectonemic or solenoidal configuration [7-9], a ribbon of small aspect ratio (width w, thickness h, aspect ratio $t = h/w << 1$, Fig. 1a-I) also displays microscopic buckling configurations [10-13], i.e., structures of size $\sim w$. For the stretched and twisted ribbon, torsion puts the edges of the ribbon under increased axial tensile stress, and axial compressive stress σ_{11} can appear in the region located close to the center of the ribbon [14-16] (helicoids, Fig. 1a-II and III). At the same time, the helical tensile stress puts the ribbon under compressive stress across the width, σ_{22}. The compressive stress causes the microscopic buckling of the twisted ribbon (a wrinkled helicoid, Fig. 1a-IV), also called longitudinal buckling [13]. With a further twisting, the ribbon forms flat triangles with sharp creases between them, the creases going in a zig-zag along the ribbon (a creased helicoid, Fig. 1a-V). At much larger torsions, macroscopic buckling occurs, similar to twisted filaments [7, 9], where the morphology transforms into a loop (Fig. 1a-VI) [13, 17], and then a cylinder (Fig. 1a-VII). Here we present a phase diagram showing the regions of the normalized torque - aspect ratio space in which the helicoid, the crease, and the cylinder are found, experimentally and theoretically, and we report the dependence of the critical torques on the tension.

We study the interaction between morphology and mechanics within the stretched and twisted ribbons, by controlling both the aspect ratio of thickness to width and the tension. Torsion experiments on polyethylene terephthalate (PET) ribbons were performed with a specially-designed torsion instrument based on the flexural pivot [18, 19], see Fig. S2. The gauge length L of each specimen is 70.00±0.50 mm; the width w is between 1.30 and 3.50 mm, and the thickness h is around 60 µm. One end of the specimen was glued to a deadweight made of two washers to give a tensile force F. The other end was reinforced by an adhesive paper backing for clamping by the upper grip. The deadweight was inserted into a U-shape lower grip mounted on the twisting head so the weight could move freely in the vertical direction. An optical microscope was used to record the morphology evolution of loaded ribbons in real time. The Young's modulus E and Poisson's ratio ν of the PET materials were determined by tensile tests, giving $E = 4.01 \pm 0.10$ GPa and $\nu = 0.40 \pm 0.01$, respectively. More experimental details are provided in the Supplementary Materials.

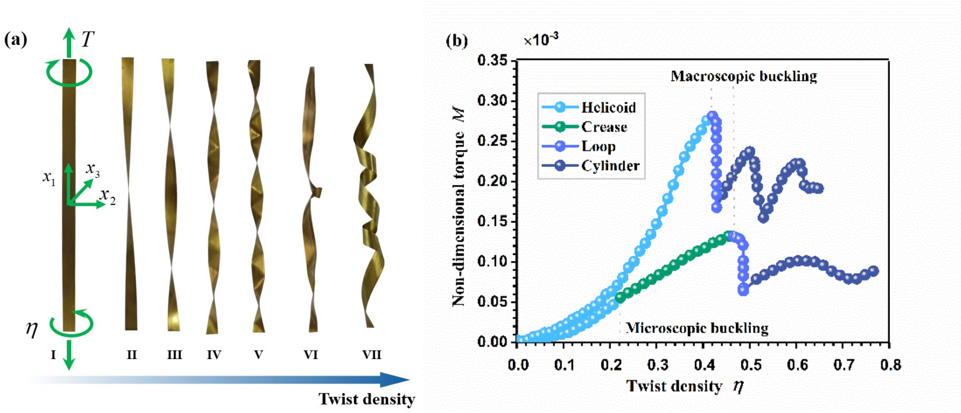

FIG. 1. (a) Morphology evolution of a twisted ribbon under a given tension: (I) Initial configuration; (II-III) Helicoid; (IV) Wrinkled helicoid; (V) Creased helicoid; (VI) Loop; (VII) Cylinder. (b) The measured torsional responses in terms of non-dimensional torque M versus twist density η. The creased stage, including the wrinkled and creased helicoid configurations, is observed in the twisted ribbon (the lower curve) with $w = 2.71 \pm 0.02$ mm and $F = 0.060$ N. The configuration of the narrow ribbon (the upper curve) with $w = 1.41 \pm 0.01$ mm and $F = 0.064$ N jumped directly from III to VI.

The morphology evolution of the stretched and twisted ribbons is shown in Fig. 1(a). The various configurations, helicoid, wrinkled helicoid, creased helicoid, loop, and cylinder, are observed in turn with increasing twist. Two typical different torsional responses are given in Fig. 1(b) for ribbons with $w = 2.71 \pm 0.02$ and 1.41±0.01 mm, respectively. The torsion values are given as non-dimensional torque M and plotted against the twist density η. Here, $M = Q/Ehw^2$ with Q being the torque, and $\eta = \theta w/L$, where θ is the torsion angle. The curves in Fig. 1(b) correspond to two different morphology evolutions. The lower curve shows microscopic buckling occurring first, where the shape develops from the helicoid, through the wrinkled helicoid, to the creased helicoid. Upon further twist, macroscopic buckling occurs with the formation of a loop at the mid-point; as the loop number increases, the cylinder configuration becomes visible (see Video S1 in Supplemental Material). The upper curve corresponds to a narrow ribbon. As the twist increases, macroscopic buckling occurs directly without microscopic buckling. The ribbon shape transforms directly from the helicoid into the loop and then the cylinder configuration (see Video S2 in Supplemental Material). The morphology transitions strongly affect the mechanical response of the twisted ribbon. The torque increases nonlinearly with the twist during the helicoid stage, but almost linearly during the crease stage. The formation of the cylindrical configuration is accompanied by a sawtooth variation of the torque with the twist. Here, the twisting energy is converted into bending energy piece by piece as the twist increases. These abrupt changes in torque coincide with the successive instabilities of the twisted ribbon.

The ribbon has been described as a two-dimensional plate [14, 20] or an inextensible rod [21, 22]. The mechanical response of the stretched and twisted ribbon has been quantitatively investigated only at the helicoid stage [23]. To study the mechanical responses and the buckling criteria of the twisted ribbon from the helicoid through the crease to the cylinder, we developed a physical model based on the energy method. The Cartesian coordinate system is defined in Fig. 1(a)-I. In what follows, the energy and work due to torsion and tension are normalized by $EhwL$. The tension T are defined by $T = F/Ehw$. The energy balance of the ribbon under tension and torsion is given by $\int M(\eta)\mathrm{d}\eta + \varOmega = \varPi^{\mathrm{el}}$, where $\varPi^{\mathrm{el}}$ is the normalized strain energy and $\varOmega$ is the normalized external work due to tension. Thus, we have $M = \partial\varPi/\partial\eta$, where $\varPi = \varPi^{\mathrm{el}} - \varOmega$ is the twisting strain energy.

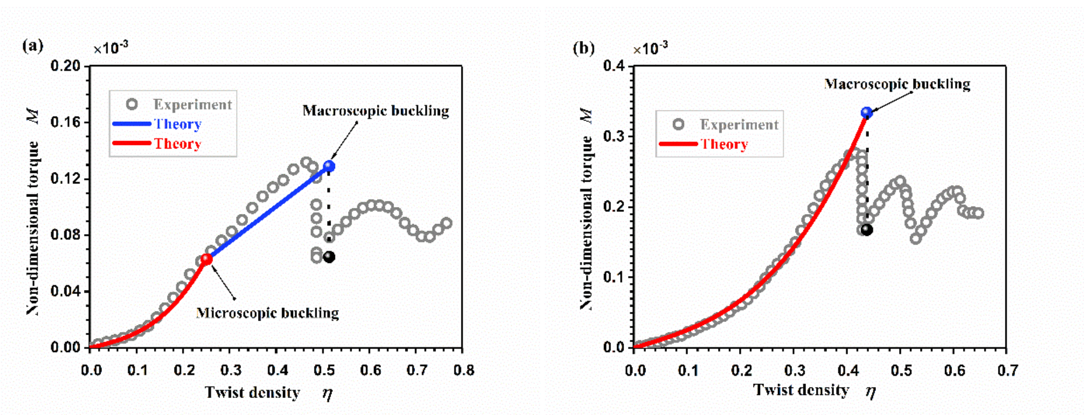

FIG. 2. Theoretical predictions of the non-dimensional torque against twist density compared with experiments. The red and blue curves are given by Eq. (2) and Eq. (4), respectively. (a)

Response of ribbon with $w = 2.71 \pm 0.02$ mm and $F = 0.060$ N. (b) Response of ribbon with $w = 1.41 \pm 0.01$ mm and $F = 0.064$ N.

Solving the Föppl–von Kàrmàn (FvK) equations by assuming the helicoid geometry [23], the elastic strain energy of the stretched and twisted ribbon is given by $\Pi_{\mathrm{hel}}^{\mathrm{el}} = \frac{1}{1440}\eta^4 + \frac{t^2}{12(1+\nu)}\eta^2 + \frac{1}{2}T^2$. The work due to tension is $\Omega_{\mathrm{hel}} = T^2 - T\eta^2/24$. The twisting strain energy for the helicoid stage is then given by

$$\Pi_{\mathrm{hel}} = \frac{1}{1440}\eta^4 + \frac{1}{12(1+\nu)}t^2\eta^2 + \frac{1}{24}T\eta^2 - \frac{1}{2}T^2. \quad (1)$$

Thus, the torque for the helicoid stage is

$$M_{\mathrm{hel}} = \frac{\partial \Pi_{\mathrm{hel}}}{\partial \eta} = \frac{1}{360}\eta^3 + \frac{t^2}{6(1+\nu)}\eta + \frac{1}{12}T\eta. \quad (2)$$

For small twists $\eta \sim 0$, $M \approx \frac{t^2}{6(1+\nu)}\eta + \frac{1}{12}T\eta$, which gives a linear description. The nonlinear behavior of torque at larger twists is well characterized by Eq. (2), as shown in Fig. 2.

As the twist density reaches a critical value η_1^*, the ribbon may undergo the microscopic buckling (wrinkling), as seen in Fig. 2(a). The creased helicoid configuration has been described as an isometric shape assuming triangular facets separated by isometric ridges [12, 24]. Here, we use the corrected Sadowsky's strain energy [25] to describe the response of the creased ribbon, i.e., $\Pi_{\mathrm{wr}}^{\mathrm{el}} = \frac{t^2\eta^2}{6(1-\nu^2)}$. This strain energy has been interpreted as a relaxed energy accounting for the occurrence of wrinkle and crease [26, 27]. The work due to tension is given by $\Omega = T\lambda$, where $\lambda = (L' - L)/L$ is the contraction with L and L' being the end-to-end distance of the ribbon at the initial and deformed configurations, respectively. The contraction can be written as[12] $\lambda = -\frac{\eta^2}{8} - \frac{\eta^4}{128} + \mathcal{O}(\eta^6)$. The twisting strain energy for the creased ribbon is then given by

$$\Pi_{\mathrm{wr}} = \left[\frac{t^2}{6(1-\nu^2)} + \frac{T}{8}\right]\eta^2. \quad (3)$$

Correspondingly, the torque is given by

$$M_{\mathrm{wr}} = \frac{\partial \Pi_{\mathrm{wr}}}{\partial \eta} = \left[\frac{t^2}{3(1-\nu^2)} + \frac{T}{4}\right]\eta . \tag{4}$$

It indicates that the torque strongly depends on t and T, and increases linearly with twisting. The theoretical prediction agrees well with the measurement, see Fig. 2(a). The critical twist density η_1^* for the microscopic buckling can be obtained by equating Π_{hel} and Π_{wr}, i.e., $\eta_1^* = \sqrt{60\left[T + t^2/(1-\nu)\right]}$. Substituting η_1^* into Eq. (2), we have the critical torque for the microscopic buckling

$$M_1^{\mathrm{cr}} = \frac{\sqrt{15}}{2}\left[T + \frac{4t^2}{3(1-\nu^2)}\right]\left(T + \frac{t^2}{1-\nu}\right)^{\frac{1}{2}} . \tag{5}$$

The microscopic buckling relaxes the axial compressive stress that appeared in the center range of the twisted ribbon. Upon further twisting, the wrinkling is insufficient to stabilize the ribbon configuration [15, 16, 28]. Once the twist density reaches the next critical value η_2^*, ribbons undergo macroscopic buckling, as seen in Fig. 2. Such a buckling is similar to the Euler buckling of a twisted filament [18, 29, 30]. For both the helicoidal and creased ribbon, the midline along the longitudinal direction goes from straight to helical. A tiny increment of twist $\Delta\eta$ leads to a localized loop at the mid-point of the specimen with an evident axial contraction. During the loop formation, the crease characteristics are retained at both ends, while the torque drops from the upper critical value M_2^{cr} to the lower one M_3^{cr}. Similar to a twisted rod, the upper critical torque can be predicted by the Timoshenko model [30],

$$M_2^{\mathrm{cr}} = t\sqrt{T/3} . \tag{6}$$

To obtain the lower critical torque M_3^{cr}, we consider the curvature radius ρ of the loop that is normalized by w (see Fig. S4 in Supplemental Material). We then have the increment of the bending strain energy for the twist increment $\Delta\eta$ during the formation of the loop, i.e., $\Delta\Pi_{\mathrm{B}} \sim \dfrac{t^2 \Delta\eta}{24\rho}$. The longitudinal contraction is associated with the curvature radius ρ and the twist density increment $\Delta\eta$, i.e., $\lambda \sim -\rho\Delta\eta$. The work due to torsion is

$\Delta\Omega_{\mathrm{Tw}} \sim M\Delta\eta$, and the work due to tension is $\Delta\Omega_{\mathrm{T}} \sim T\lambda$. From the conservation of energy, we have $\Delta\Pi_{\mathrm{B}} = \Delta\Omega_{\mathrm{Tw}} + \Delta\Omega_{\mathrm{T}}$. Differentiating the energy with respect to $\Delta\eta$, we obtain the torque

$$M \sim T\rho + \frac{t^2}{24\rho}. \tag{7}$$

Differentiating M with respect to ρ and setting the differential equal to zero, we obtain the critical curvature radius for the loop configuration $\rho \sim \frac{t}{\sqrt{24T}}$. Substituting it into Eq. (7) leads to the lower critical torque for the macroscopic buckling,

$$M_3^{\mathrm{cr}} = kt\sqrt{T}, \tag{8}$$

where k is a shape factor associated with the loop configuration. Here, $k = 0.29$ is determined by fitting the measurement data.

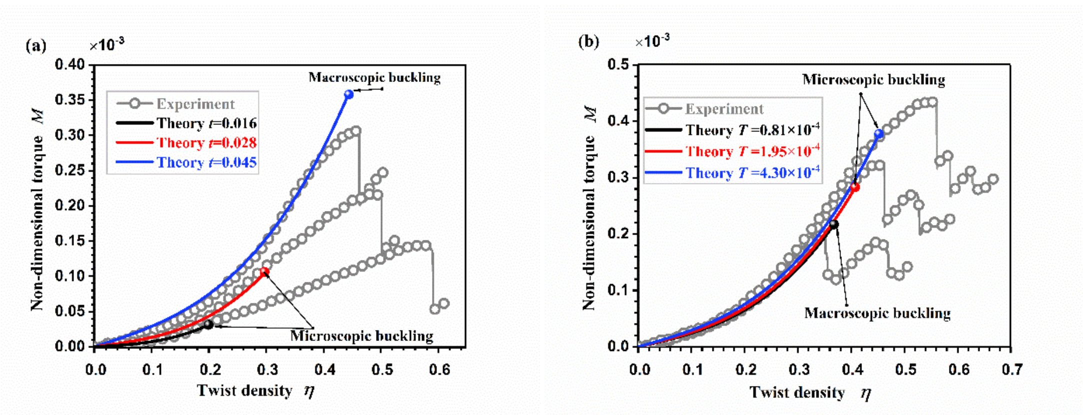

FIG. 3. Plots of the non-dimensional torque M against the twist density η. The theoretical predictions are given by Eq. (2). (a) The ribbons are under tension $T = 1.90\times10^{-4}$ with aspect ratios t = 0.016, 0.028, and 0.045. (b) The ribbons have an aspect ratio $t = 0.041$, and tensions $T = 8.10\times10^{-5}$, 1.95×10^{-4} and 4.30×10^{-4}.

Fig. 3(a) shows the normalized torque-twist curves for the ribbons with various aspect ratios t, but the same tension $T = 1.90\times10^{-4}$. By equating the critical torque for the microscopic buckling to that for the macroscopic buckling, i.e., $M_1^{\mathrm{cr}} = M_2^{\mathrm{cr}}$, one can readily obtain the critical aspect ratio t^* for a given tension. Here, our analysis gives $t^* \approx 0.043$ for the fixed tension $T = 1.90 \times 10^{-4}$. Macroscopic buckling occurs directly for the ribbon with $t = 0.045$ ($> t^*$). For the ribbons $t = 0.027$ and 0.016 ($< t^*$), microscopic buckling and then macroscopic buckling occur in turn. Fig. 3(b) shows the normalized torque-twist curves for the ribbons with different tensions, but the same aspect ratio $t = 0.041$. The curves almost overlap at the helicoid stage for different tensions. However, a slight tension change may significantly affect the instability criteria, as seen in Fig. 3(b). As the tension increases, the critical torque increases for both the microscopic and macroscopic buckling.

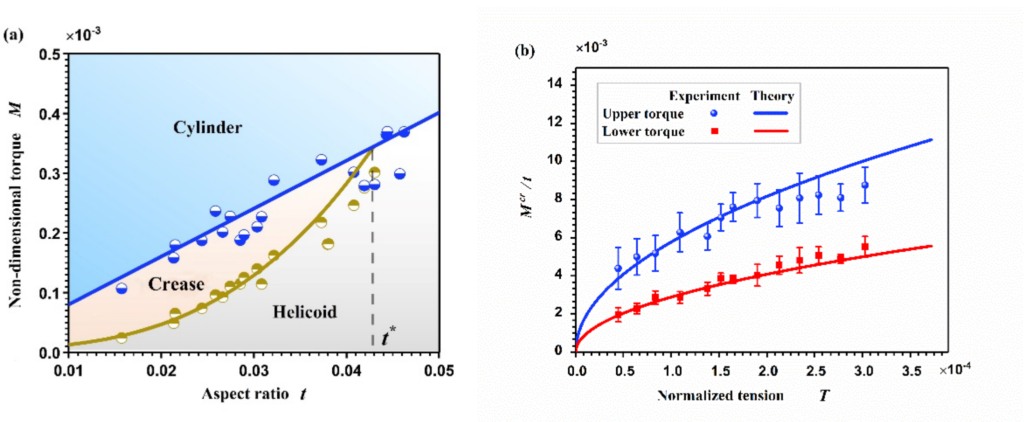

FIG. 4. The influence of the aspect ratio and the tension on the instabilities of twisted ribbons. (a) Phase diagram of twisted ribbon as a function of the torque and aspect ratio for a given tension $T = 1.90 \times 10^{-4}$. Below t^*, there are three phases, the helicoid, the crease, and the cylinder. Above t^*, there are only two phases, the helicoid and cylinder. (b) Comparison of the theoretical predictions and the experimental data for the critical torques against the tension. The solid blue and red curves are given by Eqs. (6) and (8), respectively.

A unified phase diagram of the morphologies and transitions is constructed by increasing the torque in small increments for the ribbons with different aspect ratios, as shown in Fig. 4(a). The solid red and blue curves are the theoretical predictions by Eqs. (5) and (6) for the fixed tension $T = 1.90 \times 10^{-4}$. The curves meet at a crossover point, defining the critical aspect ratio t^*. For the ribbon $t < t^*$, microscopic buckling (wrinkling) occurs first with the increase of torque; and the helicoid evolves into a creased helicoid. Upon further twist, macroscopic buckling occurs where the morphology transforms from the creased helicoid through the loop into the cylinder. For the ribbon $t > t^*$, the macroscopic buckling occurs directly, where the shape transforms from the helicoid through the loop into the cylinder. In the limit of $t = 1$, the ribbon is an elastic rod, which never wrinkles or creases.

Macroscopic buckling occurs for all ribbons with the formation of loops, and the torque drops from the upper critical value M_2^{cr} to the lower one M_3^{cr}. The comparison of the experimental results and the theoretical predictions for M^{cr} / t versus T is plotted in Fig. 4(b). The solid blue and red curves correspond to the upper and lower values of critical torque for macroscopic buckling, giving by Eq. (6) and Eq. (8), respectively. The critical torques increase nonlinearly with the tension. The theoretical predictions are in good agreement with the experimental results. As the lower critical torque corresponds to a more stable stage than the upper critical torque, the uncertainty of the lower torque measurement is much smaller than that of the upper torque measurement.

In summary, two distinct buckling histories of stretched and twisted ribbons are determined by comparing microscopic with macroscopic buckling. The way how the geometry and tension influence the morphology transitions of the twisted ribbons is elucidated. Further experimental and theoretical work is needed to map in $M - t$ and T space the morphology transitions between all the configurations and to identify any other conditions that affect these transitions.

See the **supplementary material** for video observation of the configuration transitions of the ribbons under twist and stretching, the experimental details, and the detailed theoretical derivation process.

This work was supported by the National Natural Science Foundation of China (No. 12272146 and No. 11972168), the Wuhan Application Foundation Frontier Project (No. 2020010601012174), the Fundamental Research Funds for the Central Universities (HUST: 2021JYCXJJ051), the Young Top-notch Talent Cultivation Program of Hubei Province, and the National Ten Thousand Talent Program for Young Top-notch Talents.

AUTHOR DECLARATIONS

Conflict of Interest

The authors have no conflicts to disclose.

Author Contributions

Hao Liu: Data curation (lead); Formal analysis (equal); Investigation (equal); Methodology (equal); Software (lead); Visualization (equal); Writing – original draft (equal); Writing – review & editing (equal). **Lei Liu:** Formal analysis (supporting); Data curation (supporting). **Zhi Yan:** Formal analysis (supporting); Writing – review & editing (supporting). **Yuming He:** Formal analysis (supporting); Writing – review & editing (supporting); Funding acquisition (supporting). **David J. Dunstan:** Formal analysis (supporting); Investigation (equal); Validation (equal); Writing – review & editing (equal). **Dabiao Liu:** Conceptualization (equal); Data curation (supporting); Formal analysis (equal); Investigation (equal); Methodology (equal); Software (equal); Writing – original draft (equal); Writing – review & editing (Lead); Funding acquisition (lead); Supervision (lead).

DATA AVAILABILITY

The data that support the findings of this study are available from the corresponding author upon reasonable request.

REFERENCES

[1] X. Yu, L. Zhang, N. Hu, H. Grover, S. Huang, D. Wang, and Z. Chen, Appl. Phys. Lett. **110**, 091901 (2017).

[2] Y. Yu, M. Nakano, and T. Ikeda, Nature **425**, 145 (2003).

[3] Q. Guo, A. K. Mehta, M. A. Grover, W. Chen, D. G. Lynn, and Z. Chen, Appl. Phys. Lett. **104**, 211901 (2014).

[4] S. Armon, E. Efrati, R. Kupferman, and E. Sharon, Science **333**, 1726 (2011).

[5] A. H. Gelebart, D. J. Mulder, M. Varga, A. Konya, G. Vantomme, E. W. Meijer, R. L. B. Selinger, and D. J. Broer, Nature **546**, 632 (2017).

[6] S. Srivastava *et al.*, Science **327**, 1355 (2010).

[7] N. Charles, M. Gazzola, and L. Mahadevan, Phys. Rev. Lett. **123** (2019).

[8] J. J. Wie, M. R. Shankar, and T. J. White, Nat. Commun. **7**, 13260 (2016).

[9] A. Ghatak and L. Mahadevan, Phys. Rev. Lett. **95**, 057801 (2005).

[10] D. Vella, J. Huang, N. Menon, T. P. Russell, and B. Davidovitch, Phys. Rev. Lett. **114**, 014301 (2015).

[11] T. G. Sano and H. Wada, Phys. Rev. Lett. **122**, 114301 (2019).

[12] H. Pham Dinh, V. Démery, B. Davidovitch, F. Brau, and P. Damman, Phys. Rev. Lett. **117**, 104301 (2016).

[13] J. Chopin and A. Kudrolli, Phys. Rev. Lett. **111**, 174302 (2013).

[14] A. E. Green, Proc. R. Soc. Lond. Ser. A, Math. Phys. Sci. **161**, 197 (1937).

[15] C. D. Coman and A. P. Bassom, Acta Mech. **200**, 59 (2008).

[16] J. Chopin, V. Démery, and B. Davidovitch, J. Elast. **119**, 137 (2015).

[17] O. O. Kit, T. Tallinen, L. Mahadevan, J. Timonen, and P. Koskinen, Phys. Rev. B . **85**, 085428 (2012).

[18] J. Hu, L. Liu, L. Zeng, Y. He, and D. Liu, ASME J. Appl. Mech. **89**, 051001 (2022).

[19] D. Liu， J. Hu, J. Hu, T. Luo, Z. Zhang, J. Lei, P. Hu, Y. Chen, and Y. He, Measurement, **204**, 112176 (2022).

[20] A. E. Green, Proc. R. Soc. Lond. Ser. A Math. Phys. Eng. Sci. **154**, 430 (1936).

[21] M. Sadowsky, Sitzungsber. Preuss. Akad. Wiss. **22**, 412 (1930).

[22] B. Audoly and S. Neukirch, J. Mech. Phys. Solids **153**, 104457 (2021).

[23] J. Chopin and R. T. D. Filho, Phys. Rev. E. **99**, 043002 (2019).

[24] J. Bohr and S. Markvorsen, PLoS ONE **8**, e74932 (2013).

[25] L. Freddi, P. Hornung, M. G. Mora, and R. Paroni, J. Elast. **123**, 125 (2016).

[26] A. P. Korte, E. L. Starostin, and G. H. M. Van Der Heijden, Proc. R. Soc. A **467**, 285 (2011).

[27] R. Paroni and G. Tomassetti, J. Elast. **135**, 409 (2019).

[28] M. Leembruggen, J. Andrejevic, A. Kudrolli, and C. Rycroft, arXiv preprint, arXiv:2210.14374 (2022).

[29] J. Coyne, IEEE J. Ocean. Eng. **15**, 72 (1990).

[30] S. P. Timoshenko, Theory of elastic stability, McGrow-Hill, New York,1936.

Supplemental Material for "Morphology Transitions of Twisted Ribbons: Dependence on Tension and Geometry" by Hao Liu, Lei Liu, Zhi Yan, Yuming He, David. J. Dunstan, and Dabiao Liu*.

1. Experimental details

1.1 Tensile characterization

The ribbons used here are composed of polyethylene terephthalate (PET). The tensile properties of PET ribbons are characterized using a specially-design tensile tester [1]. The dimensions and Young's modulus of the ribbon specimens for the tensile experiments are shown in Table S1. Each specimen was clamped between the upper and lower grips. The lower grip was driven by a high-resolution actuator (PI, M227.25). The upper grip was attached to a sensitive load cell. All tensile tests were performed with a strain rate well below 10^{-3}/s at room temperature. The elastic range of the typical stress-strain curves of the PET ribbons is given in Fig. S1. Here, the stress is calculated as the tensile force F over the cross-section area, and the strain is calculated as $\Delta L/L_0$. Here, ΔL is the axial displacement, and L_0 the gauge length. By fitting the stress-strain data, we obtain the Young's modulus $E = 4.01 \pm 0.10$ GPa. The Poisson's ratio $\nu = 0.40 \pm 0.01$ is measured by the digital image correlation (DIC) method.

Table S1. Geometrical parameters and Young's modulus of the PET ribbons.

Parameters	Width w (mm)	Thickness h (μm)	Gauge length L_0 (mm)	Young's modulus E (GPa)
Values	4.71±0.09	61.1±1.8	10.0±0.2	4.01±0.10

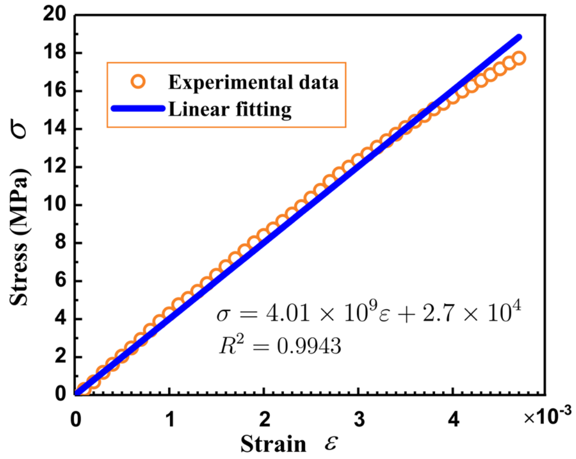

Fig. S1 Tensile stress-strain curves of the PET ribbons. The Young's modulus is obtained by a linear fitting (blue line).

1.2 Micro-torsion instrument

The torsional behaviors of PET ribbons under tension are characterized using a homemade torsion tester for small-scale components based on the flexural pivot, as shown in Fig. S2. The design is inspired by the work of Hu et al. [2], which deals with the torsional properties of soft filaments and other slender structures. The morphology of each PET ribbon was observed by a 3D super-depth digital microscope (KEYENCE VHX-500FE). The detail on the torsion instrument has been provided in Ref. [3].

The crucial part of the instrument is the torque transducer, incorporating a cylindrical flexural pivot, a shim bonded to the sleeve of the pivot, and a sensitive angle detector. The cylindrical flexural pivot (C-Flex Bearing Co. Inc.) with a suitable torsional stiffness acts as the sensor element, as illustrated in Fig. 2. The flexural pivot is produced by joining two thin beams that rotate via relatively thin flexures. The flexures are positioned so that their planes are normal with each other. Their intersection is on the desired axis of rotation. One end of the pivot is fixed to a three-dimensional translation stage, while the other is connected to a grip. Twisting the pivot results in bending the flexure beam, and hence the tilt angle of the shim is equal to the angular displacement of the pivot. The torsion angle of the flexural pivot φ is measured accurately with an optical angle detector involving dual laser displacement sensors. If the torsional spring constant of the flexural pivot, K, is given, the torque Q acting on the specimen can directly be deduced, i.e.,

$$Q = K\varphi . \tag{S1}$$

The ribbon is suspended from the torque transducer. The lower end of the specimen is bonded to a deadweight. The deadweight provides an array of the desired extension to the specimen. The deadweight is put into a slot of the twisting head to prevent lateral movement while allowing it to slide freely in the vertical direction. A stepper motor is used to twist the ribbon specimen. An in-situ optical microscope consisting of a CCD camera is used to monitor the deformation of the ribbon in real time.

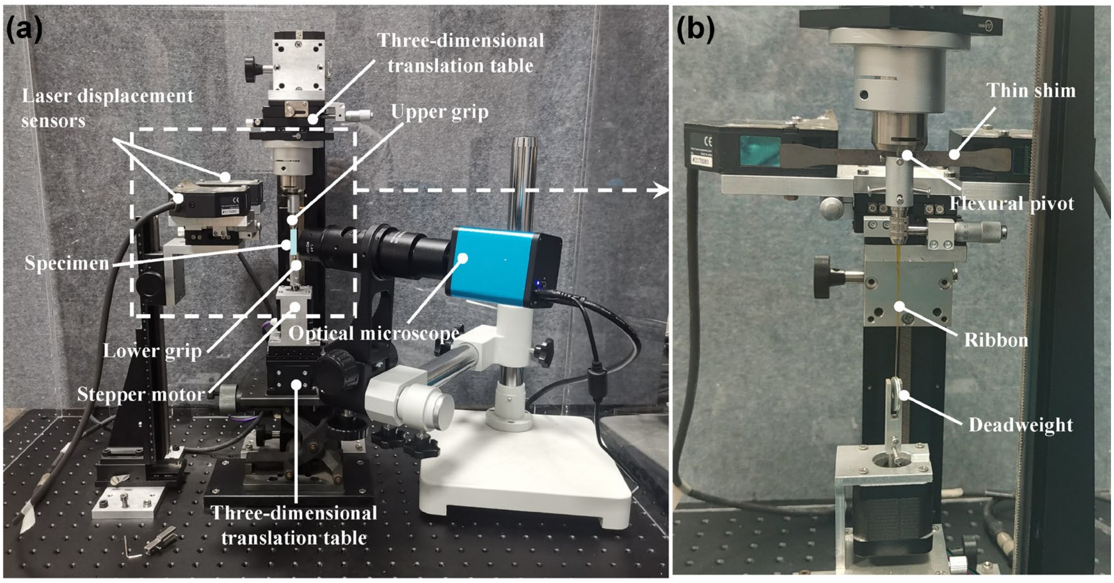

Fig. S2. Schematics of the torsion instrument [3].

1.3 Torsional responses

Typical experimental curves of non-dimensional torque M versus twist density $\eta = \theta w / L$ are shown in Fig. S3. The twisted ribbons, under constant tension, generally transform from the helicoid through the crease to the loop and then to the cylinder. In Fig. S3(a), microscopic buckling and macroscopic buckling occur in turn. In contrast, in Fig. S3(b), the macroscopic buckling occurs directly without the microscopic buckling. That is, the wrinkled and creased helicoid configurations vanish.

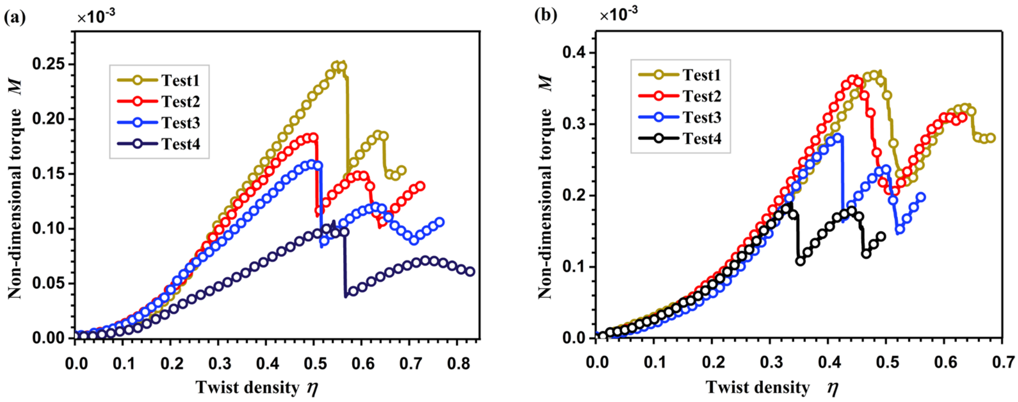

Fig. S3. Typical experimental curves of non-dimensional torque against twist density. (a) The tension varies from 3.05×10^{-4}, 1.90×10^{-4}, 1.63×10^{-4}, to 1.17×10^{-4} and the aspect ratio varies from 0.025, 0.028, 0.022, to 0.016 for the test 1-4, respectively. (b) The tension varies from 1.91×10^{-4}, 1.78×10^{-4}, 1.23×10^{-4}, to 0.85×10^{-4} and the aspect ratio varies from 0.046, 0.044, 0.042, to 0.045 for the test 1-4, respectively.

2. Theoretical analysis

The longitudinal and transverse coordinates in the initial configuration are denoted as x_1 and x_2, respectively; they vary in the ranges $-L/2 \le x_1 \le L/2$ and $-w/2 \le x_2 \le w/2$. The orientation of x_3- axis of the Cartesian coordinate system (x_1, x_2, x_3) is normal to the ribbon surface, which varies in the range $-h/2 \le x_3 \le h/2$.

The energy balance of the twisted ribbon under a given tension is expressed as

$$\int Q(\theta)d\theta + \Gamma = \Psi^{\mathrm{el}}, \tag{S2}$$

where Γ is the work due to tension, and Ψ_{el} is the strain energy. Thus, we obtain the torque

$$Q = \frac{\partial \Psi}{\partial \theta}, \tag{S3}$$

where $\Psi = \Psi^{\mathrm{el}} - \Gamma$ is the twisting strain energy.

2.1 The helicoid stage

We adopt the nonlinear Föppl–von Kàrmàn (FvK) equations to describe the ribbon [4], i.e.,

$$D\nabla^4 w = h\left(\Phi_{,11}u_{,22} + \Phi_{,22}u_{,11} - 2\Phi_{12}u_{,21}\right) \tag{S4}$$

and

$$\nabla^4 \Phi = E\left[\left(u_{,12}\right)^2 - u_{,11}u_{,22}\right], \tag{S5}$$

where Φ is the Airy stress function, $u = u(x_1, x_2)$ is the deflection of the ribbons at x_3 direction. The comma in subscript denotes the partial derivation to $x_i\,(i=1,2)$. The strain energy Ψ^{el} is composed of the stretching part Ψ_{S} and the bending part Ψ_{B} [4]. The stretching energy in terms of the stress σ_{ij} and strain ε_{ij} is given by

$$\Psi_{\mathrm{S}} = \frac{1}{2}\int\left(\sigma_{11}\varepsilon_{11} + \sigma_{22}\varepsilon_{22} + 2\sigma_{12}\varepsilon_{12}\right)\mathrm{d}V . \tag{S6}$$

We assume that the materials are homogeneous, linear elastic, and isotropic. Therefore, $\varepsilon_{ij} = \frac{1}{E}\left[(1+\nu)\sigma_{ij} - \nu\sigma_{kk}\delta_{ij}\right]$ $(i, j = 1,2)$, where δ_{ij} is the Kronecker delta. Substituting it into Eq. (S6) yields

$$\Psi_{\mathrm{S}} = \frac{1}{2E}\int\left[\sigma_{11}^2 + \sigma_{22}^2 - 2\nu\sigma_{11}\sigma_{22} + 2(1+\nu)\sigma_{12}^2\right]\mathrm{d}V . \tag{S7}$$

The bending energy is given by

$$\Psi_{\mathrm{B}} = \frac{Eh^3}{24(1-\nu^2)}\iint\left(u_{,11} + u_{,22}\right)^2 - 2(1-\nu)\left(u_{,11}u_{,22} - u_{,12}^2\right)\mathrm{d}x_1\mathrm{d}x_2 . \tag{S8}$$

The deflection is assumed by

$$u\left(x_1, x_2\right) = \tau x_1 x_2 , \tag{S9}$$

where $\tau = \theta/L$ is the twisting rate. Then, Eq. (S5) can be simplified as $\frac{\partial^4\Phi}{\partial x_2^4} = E\tau^2$. Integrating this formula gives

$$\Phi = \frac{E}{24}\tau^2 x_2{}^4 + \frac{C_1}{6}x_2{}^3 + \frac{C_2}{2}x_2{}^2 + C_3 x_2 + C_4 . \tag{S10}$$

The stress components given by the relation with the Airy function are

$$\sigma_{11} = \frac{\partial^2\Phi}{\partial x_2{}^2}, \sigma_{22} = \frac{\partial^2\Phi}{\partial x_1{}^2}, \sigma_{12} = -\frac{\partial^2\Phi}{\partial x_1\partial x_2} . \tag{S11}$$

We assume that the stress field is invariant along the x_1 direction. The stress fields read

$$\sigma_{22} = \sigma_{12} = 0, \quad \sigma_{11} = \frac{E}{2}\tau^2 x_2{}^2 + C_1 x_2 + C_2 . \tag{S12}$$

As σ_{11} is symmetric along the x_2 direction of the ribbons, the constant $C_1 = 0$. We follow Chopin and Filho [5] and assume $C_2 = E\lambda$. Here, the parameter $\lambda = \left(L' - L\right)/L = \Delta L/L$ is the contraction with L and L' being the ribbon length at the initial and the deformed configurations, respectively.

$$\sigma_{11} = E\left(\frac{\tau^2 x_2{}^2}{2} + \lambda\right) \tag{S13}$$

By the equilibrium condition $F = h\int_{-w/2}^{w/2} \sigma_{11} \mathrm{d}x_2$, the contraction for the helicoid reads [5]

$$\lambda_{\mathrm{hel}} = \frac{F}{Ehw} - \frac{w^2\tau^2}{24} \tag{S14}$$

Substituting the stress components and deflection into Eq. (S7) and Eq. (S8), we have the strain energy for the helicoid

$$\Psi_{\mathrm{hel}}^{\mathrm{el}} = \frac{Eh\tau^4 w^5 L}{1440} + \frac{Eh^3 w\tau^2 L}{12(1+\nu)} + \frac{F^2 L}{2Ehw}. \tag{S15}$$

The work due to tension is given by

$$\Gamma_{\mathrm{hel}} = F\Delta L = FL\left(\frac{F}{Ehw} - \frac{w^2\tau^2}{24}\right), \tag{S16}$$

Therefore, we obtain the twisting strain energy of the ribbon at the helicoid stage

$$\Psi_{\mathrm{hel}} = \frac{Eh\tau^4 w^5 L}{1440} + \frac{Eh^3 w\tau^2 L}{12(1+\nu)} + \frac{Fw^2\tau^2 L}{24} - \frac{F^2 L}{2Ehw}. \tag{S17}$$

We use w as a unit of length, and Eh as a unit of in-plane stress, and introduce the twist density $\eta = \theta w/L$. Further, the aspect ratio t and tension T can be defined as $t = h/w$ and $T = F/Ehw$, respectively. The energy and work due to torsion and tension can be normalized by $EhwL$, i.e., $\Pi = \Psi/EhwL$ and $\Omega = \Gamma/EhwL$. The normalized twisting strain energy is

$$\Pi_{\mathrm{hel}} = \frac{\Psi_{\mathrm{hel}}}{EhwL} = \frac{1}{1440}\eta^4 + \frac{1}{12(1+\nu)}t^2\eta^2 + \frac{1}{24}T\eta^2 - \frac{1}{2}T^2. \tag{S18}$$

Therefore, the normalized torque M for the helicoid is given by

$$M = \frac{Q}{Ehw^2} = \frac{\partial \Pi_{\mathrm{hel}}}{\partial \eta} = \frac{1}{360}\eta^3 + \frac{t^2}{6(1+\nu)}\eta + \frac{1}{12}T\eta. \tag{S19}$$

2.2 The crease stage

The corrected Sadowsky's strain energy[6] can be written as the function of bending κ_2 and twisting curvature κ_3, i.e.,

$$
\Psi_{\mathrm{wr}}(\kappa_2,\kappa_3)=\begin{cases}\dfrac{Ewh^3L}{24(1-\nu^2)}\dfrac{(\kappa_2^2+\kappa_3^2)^2}{\kappa_2^2} & \text{if } |\kappa_3|\leqslant|\kappa_2| \\ \dfrac{Ewh^3L\kappa_3^2}{6(1-\nu^2)} & \text{if } |\kappa_3|\geqslant|\kappa_2|\end{cases}. \tag{S20}
$$

For the creased helicoid, we have $|\kappa_3|\geqslant|\kappa_2|$. Here, $\tau=\kappa_3=\theta/L$. Therefore, the strain energy of the twisted ribbon at the crease stage is given by

$$
\Psi_{\mathrm{wr}}^{\mathrm{el}}=\frac{Ewh^3L}{6(1-\nu^2)}\tau^2. \tag{S21}
$$

The contraction for the creased ribbon can be written as $\lambda_{\mathrm{wr}}=-\frac{\eta^2}{8}-\frac{\eta^4}{128}+\mathcal{O}(\eta^6)$ [7]. The twisting strain energy of the creased ribbon is

$$
\Psi_{\mathrm{wr}}=\frac{Ewh^3L\tau^2}{6(1-\nu^2)}+F\left(\frac{w\tau^2}{8}+\frac{w^4\tau^4}{128}\right)L+\mathcal{O}(\tau^6). \tag{S22}
$$

Only retain square terms of τ, the normalized twisting strain energy is

$$
\Pi_{\mathrm{wr}}=\frac{\Psi_{\mathrm{wr}}}{EhwL}=\left[\frac{t^2}{6(1-\nu^2)}+\frac{T}{8}\right]\eta^2 \tag{S23}
$$

The normalized torque is given by

$$
M=\frac{Q}{Ehw^2}=\frac{\partial\Pi_{\mathrm{hel}}}{\partial\eta}=\left[\frac{t^2}{3(1-\nu)}+\frac{T}{4}\right]\eta. \tag{S24}
$$

2.3 Analysis of the loop configuration

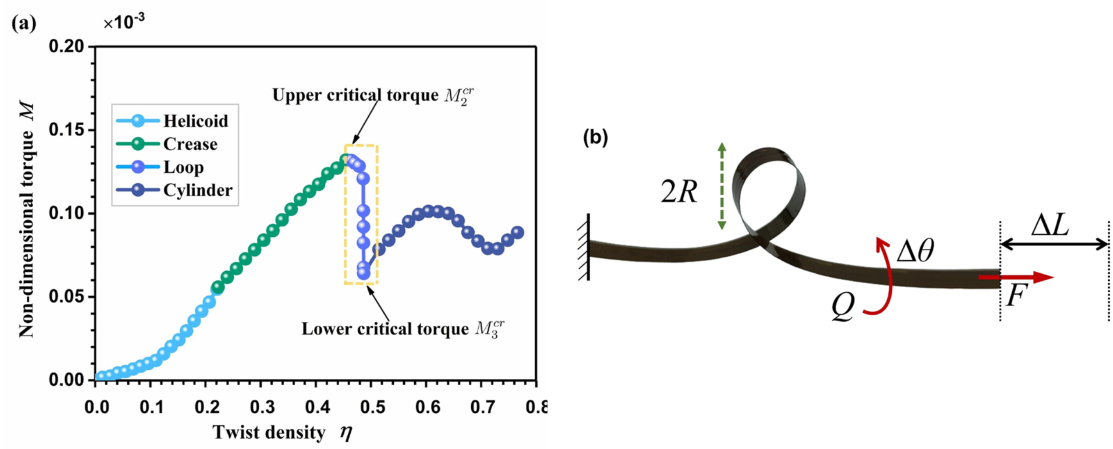

Fig. S4. Analysis of the loop configuration. (a) The mechanical response during the loop formation highlights a box in yellow. The torque drops from an upper critical value M_2^{cr} to a lower critical value M_3^{cr}. (b) The schematic diagram of the loop for the ribbon.

For a tiny incremental twist angle $\Delta\theta$, we obtain the increased bending strain energy for the loop [8]

$$\Delta \Psi_{B} = \frac{1}{2}EI\int_{Loop}\frac{1}{R^2}\mathrm{d}S \sim \frac{1}{2}EI\frac{1}{R^2}\Delta L \quad \text{(S25)}$$

where $I = \frac{h^3 w}{12}$ is the geometric moment of inertia. The external works due to tension and twist are given by $\Delta\Gamma_{T} \sim F\Delta L$ and $\Delta\Gamma_{Tw} \sim Q\Delta\theta$, where $\Delta L \sim -R\Delta\theta$. Based on the law of energy conservation, we have

$$\Delta \Psi_{B} = \Delta\Gamma_{Tw} + \Delta\Gamma_{T}\,. \quad \text{(S26)}$$

Differentiating two sides of the energy equilibrium Eq. (S26) with respect to $\Delta\theta$, we have the torque

$$Q \sim FR + \frac{1}{2R}EI\,. \quad \text{(S27)}$$

Differentiating Q with respect to R, setting the differential equal to 0, we obtain the critical curvature radius for the loop configuration i.e., $R \sim \sqrt{EI/2F}$. Substituting it into Eq. (S27), the lower critical torque for the macroscopic buckling is

$$M_3^{cr} = \frac{Q_3^{cr}}{Ehw^2} = kt\sqrt{T}\,, \quad \text{(S28)}$$

where k is a shape factor associated with the loop configuration. Here, $k = 0.29$ is determined by fitting the measurement data.

3. Supplemental Movies

Supplemental Movie 1

The normalized torque-twist curve is obtained by experiment. The shape is developed from the helicoid through the wrinkled helicoid to the creased helicoid. Upon further twist, macroscopic buckling occurs with the formation of a loop at the mid-point, and then as the loop number increases, the cylinder configuration is recognized. The ribbon specimens used here are of length $L = 70.12$ mm, width $w = 2.21$ mm, and thickness $h = 62.24$ μm. It is twisted by an angle θ and stretched longitudinally by a fixed force $F = 0.091\text{N}$.

Supplemental Movie 2

The ribbon specimens are of length $L = 69.54$ mm, width $w = 1.34$ mm, thickness $h = 60.02$ μm, and stretched longitudinally by a fixed force $F = 0.032\text{N}$. As the twist increases, the ribbon shape transforms directly from the helicoid into the loop and then the cylinder configuration.

Supplemental Movie 3

The ribbon specimen is of length $L = 70.40$ mm, width $w = 3.10$ mm, and thickness $h = 62.18$ μm, and stretched longitudinally by a fixed force $F = 0.137$ N. The crease stage is more evident as the width and tension increase.

REFERENCES

[1] D. Liu, Y. He, P. Hu, and H. Ding, Exp. Mech. **57**, 297 (2017).

[2] J. Hu, L. Liu, L. Zeng, Y. He, and D. Liu, ASME J. Appl. Mech. **89**, 051001 (2022).

[3] D. Liu，J. Hu, J. Hu, T. Luo, Z. Zhang, J. Lei, P. Hu, Y. Chen, and Y. He, Measurement, **204**, 112176 (2022).

[4] D. O. Brush, B. O. Almroth, and J. Hutchinson, Buckling of bars, plates, and shells. 911 (1975).

[5] J. Chopin and R. T. D. Filho, Phys. Rev. E. **99**, 043002 (2019).

[6] L. Freddi, P. Hornung, M. G. Mora, and R. Paroni, J. Elast. **123**, 125 (2016).

[7] H. Pham Dinh, V. Demery, B. Davidovitch, F. Brau, and P. Damman, Phys. Rev. Lett. **117**, 104301 (2016).

[8] A.L. Ross, Cable Kinking Analysis and Prevention, ASME J. Eng. Ind. **99**, 920 (1977).